Journal of Electric Propulsion

RESEARCH Open Access

Molecular Dynamics Simulations of Ion Extraction from Nanodroplets for Ionic Liquid Electrospray Thrusters

Takaaki Enomoto[1], Shehan M. Parmar[2*], Ryohei Yamada[3,4], Richard E. Wirz[2] and Yoshinori Takao[5*]

*Correspondence: parmar@ucla.edu; takao@ynu.ac.jp

[1] Department of Mechanical Engineering, Materials Science, and Ocean Engineering, Yokohama National University, Yokohama 240–8501, Japan
[2] Department of Mechanical and Aerospace Engineering, University of California, Los Angeles, 420 Westwood Plaza, Los Angeles 90095, CA, USA
[3] College of Engineering Science, Yokohama National University, Yokohama 240–8501, Japan
[4] Present Address: Department of Physics, The University of Tokyo, Tokyo 113–0033, Japan
[5] Division of Systems Research, Yokohama National University, Yokohama 240–8501, Japan

Abstract

Molecular dynamics (MD) simulations were performed for ion extraction from electrospray thrusters to investigate relevant extraction processes numerically. To approximate the electrospray jet tip, a simulation domain consisting of 4-5 nm-sized ionic liquid droplets was used. The extracted ion angles and kinetic energies from EMI–BF_4 (1-ethyl-3-methylimidazolium tetrafluoroborate) and EMI–Im (1-ethyl-3-methylimidazolium bis((trifluoromethyl)sulfonyl)imide) droplets were quantified by applying uniform electric fields of 1.3–1.7 V nm^{-1}. The MD simulations are in great agreement with simulations presented in the literature and consistently show a greater preference for monomer emission than reported experimentally. At field strengths above 1.5 V nm^{-1}, apparent droplet fracturing and breakup lead to an increase in ion angular velocity distributions. Greater mobility of EMI–BF_4 ions than EMI–Im was also observed, indicative of the crucial role of cation-anion hydrogen bond strengths in ion extraction and beam composition between different propellants.

Keywords: Electrospray, Ionic liquids, Molecular dynamics

Introduction

Recently, nanosatellite operations have been rapidly increasing because of their lower costs and shorter development periods compared to conventional, large satellites [1, 2]. For advanced missions, such as satellite constellations and deep space exploration, nanosatellites need propulsion systems for orbital maneuvers and attitude control [3]. To this end, nanosatellites require propulsion systems that can achieve tight positioning control, low thrust/high I_{sp}, and low power consumption within an allocated mass and size budget [4]. Among the various electric propulsion systems used today, such as Hall thrusters, gridded ion thrusters (GIT), or pulsed plasma thrusters (PPTs), ionic liquid electrospray thrusters (ILESTs) could further increase nanosatellite payload capabilities because of their small size and flexible operating modes [5, 6].

Figure 1 shows a schematic of the electrospray thruster, which mainly consists of an emitter array and an extractor electrode. Applying a high voltage between the emitter and extractor enables the ionic liquid to reach the emitter tip by the electric force, forming a Taylor cone [7]. When the local electrostatic pressure at the emitter tip

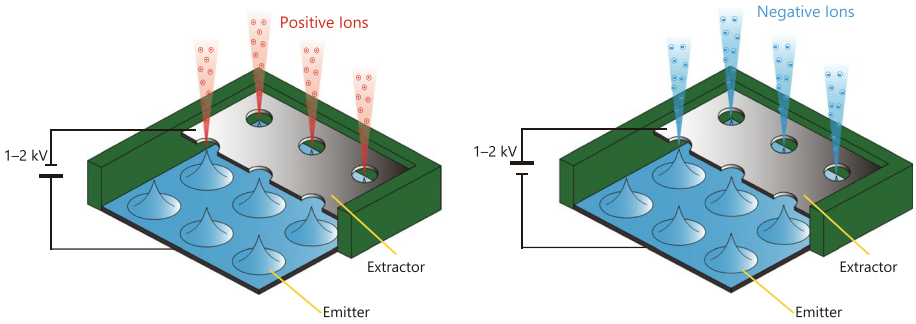

Fig. 1 Schematic of the electrospray thruster

exceeds an internal pressure by the surface tension of the ionic liquid, ions or droplets are extracted and accelerated, and then the thrust is provided to a spacecraft [8]. ILESTs can operate as either ionic liquid ion sources (ILIS) [9], where propellant is passively fed through an externally wetted emitter or porous material [10, 11] to emit purely monomer ions, or a droplet-dominated emission mode, where propellant is actively fed through a capillary emitter [12].

Ionic liquids contain only anions and cations without solvent. The vapor pressure of ionic liquids is almost zero because of the strong Coulomb force between cations and anions [13, 14], indicating that ionic liquids can stay as a liquid phase even in space. As opposed to gridded ion and Hall thrusters, during bi-polar pulse high voltage electrospray operation, both anions and cations can be extracted such that no neutralizers are required [15]. High-pressure gas storage and feeding systems are also unnecessary for ILESTs. These features allow the entire propulsion system to be miniaturized significantly compared to other electric propulsion systems, thus enabling concepts like staging of entire thruster modules or multiplexing of ILEST emitters for improved redundancy and scalability [3, 16]. Moreover, droplet-mode ILEST technologies, such as the Colloid Micronewton Thrusters (CMNTs) on-board the LISA Pathfinder technology demonstration, exhibit key mission capabilities such as micronewton thrust precision and low thrust-noise. [17, 18]

Previous studies indicated that some of the divergent ion beams collided with the extractor, which could erode the extractor [19–21]. To prevent extractor erosion, we have investigated trajectories of ion beams extracted from the emitter tip using particle-in-cell (PIC) simulations [22]. However, we found that the initial conditions at the emitter tip, such as the kinetic energy and the extracted angles, strongly affected ion trajectories, where the kinetic energy and the extracted angles had to be assumed in the particle simulations.

This observation, that charged particle trajectories are most sensitive to initial ion kinetic energies and extraction angles, is corroborated by similar electrospray plume models and experiments. For instance, Nuwal et al. [23] conducted 3D-PIC simulations using an unstructured adaptive automatic mesh refinement/octree grid to show the large electric field gradients near the emitter, spanning multiple orders of magnitude in length scale. It follows that the electric potential energy is equal to the kinetic energy of a charged particle at the site of emission. Furthermore, previous retarding

potential analyzer (RPA) experiments have shown that variations in initial ion emission energy can influence the spacing between the cation-anion pairs. Past a certain energy threshold, the cation and anion molecules may overcome their attractive Coulomb forces, resulting in ion cluster dissociation or fragmentation of downstream solvated ion clusters [24, 25]. Furthermore, Gamero-Castaño [26] implemented an Eulerian electrospray beam model based on the line-of-point-charges approach and demonstrated a strong dependence of charged droplet trajectories on their initial velocities. Parmar et al. [27] conducted a variance-based, global sensitivity analysis on the inputs for a reduced-order, electrospray plume model and concluded that a particle's final position is most sensitive to other conditions such as its initial emission angle by orders of magnitude relative to its initial position and the electrode voltage. Thus, the primary objective of this work is to investigate the kinetic energy and the extracted angles at the emitter tip. To this end, we have conducted molecular dynamics (MD) simulations, which can analyze the physical motions of atoms and molecules.

MD simulations are widely used for many advanced applications [28–33] or for obtaining basic physical parameters, such as electrical conductivity [34], surface tension [35], viscosity [36], diffusion coefficient [37], and wettability [38]. They are also employed for ion extraction of electrospray thrusters because electrospray phenomena occur on an atomic scale [35, 39–43]. However, because the scale is a few orders of magnitude smaller than the real scale electrospray thrusters, MD simulations are time-consuming. To reduce calculation time, coarse-grained (CG) models have also been investigated by representing an ionic liquid molecule by only treating groups of atoms instead of each individual atom [34, 41, 42]. While CG models can achieve length-scales of up to a few 10s of nanometers, it is extremely small compared with a typical capillary scale of a few micrometers.

Our approach is similar to the work by Prince et al. [44], where a droplet of 4 nm in diameter is simulated by an all-atom model, not by coarse-grained approaches. As mentioned in their paper, the droplet simulations do not probe the interaction between ionic liquid and electrodes, but can estimate the jet's tip, which leads to droplet fission or evaporation. Moreover, nanodroplets often exit in the acceleration region, where a high electric field is applied between the emitter and extractor electrodes. In the following study, we investigate the kinetic energy and extracted angle of anions and cations that are extracted from a 4–5 nm droplet under a uni-directional uniform electric field condition. The following section describes our numerical model. In "Results & discussion" section, numerical results are shown, where we employ two types of ionic liquids, EMI–BF_4 (1-ethyl-3-methylimidazolium tetrafluoroborate) and EMI–Im (1-ethyl-3-methylimidazolium bis((trifluoromethyl)sulfonyl) imide), and focus on the position, angle, and energy of extracted ions. Finally, conclusions are drawn in "Conclusion" section.

Simulation methods

Molecular dynamics overview

Molecular dynamics can simulate atomic-scale phenomena, which consider intramolecular and intermolecular forces. In MD simulations, we calculate three-dimensional

equations of motion to obtain the positions and velocities of each atom. Forces used in the equation of motion are derived from the differential equations of the potential:

$$F_i = -\frac{\partial \phi(r_i)}{\partial r_i}, \tag{1}$$

where ϕ is the interaction potential of the molecular system and F_i and r_i are the force and position of the ith atom, respectively. In this study, all the MD simulations were carried out using the Large-scale Atomic/Molecular Massively Parallel Simulator (LAMMPS) package [45]. A Package for Building Initial Configurations for Molecular Dynamics Simulations (Packmol) is also used for the molecular arrangement during the setting of the input files [46]. Packmol implements an optimal packing algorithm that can speed up system equilibration and thermalization [47].

The interaction potential, which is necessary for Eq. 1, consists of intramolecular and intermolecular potentials that can be described by the following functional form:

$$\begin{aligned}\phi = & \sum_{bonds}^{N} k_r(r_{ij} - r_0)^2 + \sum_{angles}^{N} k_\theta(\theta_{ijk} - \theta_0)^2 \\ & + \sum_{dihedrals}^{N} k_\phi\left[1 + \cos\left(n\phi_{ijkl} - \delta\right)\right] \\ & + \sum_{i=1}^{N-1}\sum_{j>i}^{N} s_{ij}\left(4\epsilon_{ij}\left[\left(\frac{\sigma_{ij}}{r_{ij}}\right)^{12} - \left(\frac{\sigma_{ij}}{r_{ij}}\right)^{6}\right] + \frac{1}{4\pi\epsilon_0}\frac{q_i q_j}{r_{ij}}\right).\end{aligned} \tag{2}$$

The intramolecular potential models the molecule's structure, where k_r, k_θ, and k_ϕ, are the corresponding bond, angle, dihedral angle force constants, r is the distance between atoms attached by covalent bonds, θ is the angle within three atoms connected by covalent bonds, and the torsional angles are formed on two planes that include more than three molecules, where ϕ is the dihedral angle based on four atoms connected in a sequence. The dihedral angle potential also includes an integer value representing the multiplicity or number of local minima in a complete rotation about bond j—k, n, and the associated phase factor, δ. Figure 2 depicts the physical significance of each term as it relates to the cations and anions used in this work [48].

The intermolecular potential determines the structure and the movement of the overall population of molecules in the system and accounts for four intermolecular interactions: electrostatic, induced, dispersion force, and repulsive. In MD simulations, the four interactions are approximately divided into long-range and short-range interactions. As given by Eq. 2, the Coulomb potential is used for the long-range interaction, and the 12-6 Lennard-Jones (LJ) potential is used for the short-range interaction, where ε_{ij} is the potential depth, σ_{ij} is the distance between atoms i and j at which the potential reaches zero, and s_{ij} is an empirically-determined scaling factor. Because the long- and short-range interactions indicate that the potential vanishes only at infinity, we need to define a certain distance within which the potential affects the atoms, i.e., the cutoff distance. The values of the cutoff distance are shown in "Nanodroplet simulation procedure and equilibration" section. To reduce the computational cost of intermolecular interactions, only two-body interactions are calculated in this study. The potential between N atoms

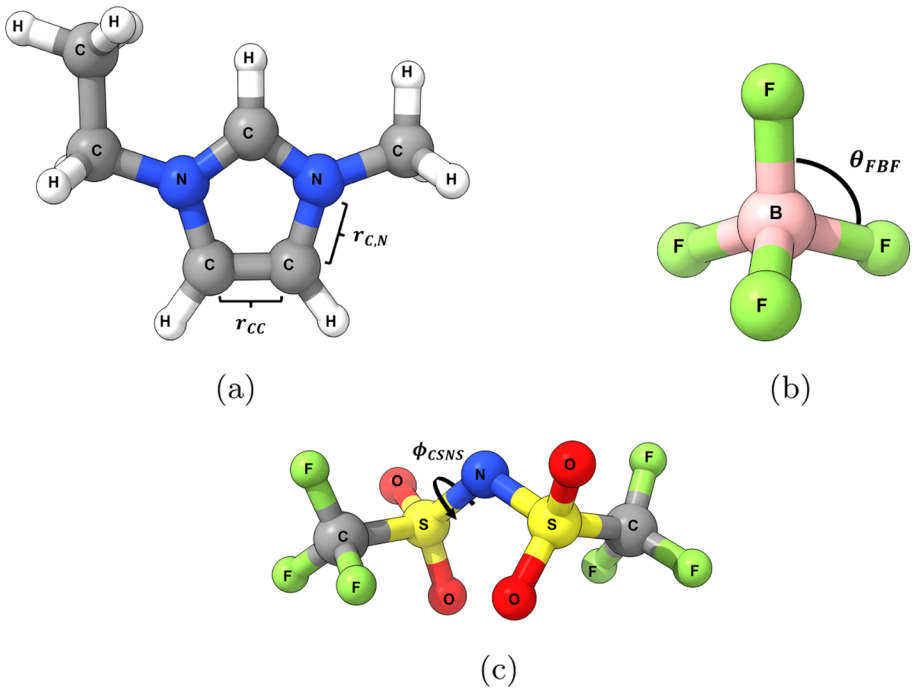

Fig. 2 Visual aid of terms in Eq. 1, where representative bonds, angles, and dihedral angles are shown in the (**a**) EMI^+ cation, (**b**) BF_4^- anion, and (**c**) EMI–Im anion often denoted as Tf_2N, respectively

is calculated by adding the potential between two atoms, thus reducing the number of interactions to ${}_nC_2 = N(N-1)/2$. Additionally, intermolecular interactions were neglected (i.e., $s_{ij}=0$) for covalently bound atoms separated by up to two bonds, scaled down by 50% (i.e., $s_{ij}=0.5$) for atoms separated by three bonds, and fully considered for atoms separated by four or more bonds (i.e., $s_{ij}=1.0$).

In order to accurately calculate all the relevant forces acting on molecules and atoms in a system, selecting the proper force field, which refers to the functional form of the interaction potential and the empirical parameters therein, is one of the most critical factors in MD simulations. In previous MD investigations of ionic liquids for electrospray propulsion applications, a wide range of force fields have been tested. For example, the effective-force coarse-graining (EFCG) model [49] has achieved significant reductions in computing time for mesoscale EMI–BF_4 simulations [34, 37, 39] by replacing the cations and anions to their most essential functional groups (i.e., the imidazolium ring, the CH_2 and CH_3 in the alkyl chains, or the entire BF_4). Despite achieved computational savings, CG models have shown difficulties in reproducing basic ionic liquid properties. To this end, all-atom force fields have been used instead and follow the most common Class I force fields: AMBER [34, 50, 51], CHARMM [44, 52], and OPLS [39]. Class I force fields typically follow the functional form given in Eq. 2 and can model a wide range of condensed-phase, organic systems [48]. Since the initial use of MD for imadazolium-based ionic liquids, significant research has been dedicated towards obtaining the most accurate set of Class I force field parameters, either by experimental techniques or *ab initio* or density functional theory (DFT) calculations [53]. At the cost of additional

runtime, higher-fidelity polarizable [54] and reactive force [55] fields are capable of accounting for more complex physical interactions, such as locally induced dipole moments or thermal decomposition, respectively. In this study, we used the Optimized Potentials for Liquid Simulations-All Atom (OPLS-AA) force field, one of the general potentials developed for organic liquids [56]. The scaling factor s_{ij} for the long-range interactions in Eq. 2 is defined by results from Lopes et al. [57].

Nanodroplet simulation procedure and equilibration

We employed 125 EMI–BF_4 and 125 EMI–Im molecules as a droplet of approximately 4–5 nm in diameter, which was assumed to be the diameter of the jet's tip or meniscus [58]. We analyzed ion extraction by applying a uniform electric field of 1.3–1.7 V nm^{-1}, which is enough to extract ions, assuming EMI–BF_4 and EMI–Im droplets were placed in a vacuum without gravity.

Before applying the electric field, we equilibrated the droplet for 300–400 ps from the initial condition using the canonical (NVT) ensemble at T= 300 K. The initial velocity of each atom was set randomly to satisfy the Gaussian distribution, and a Nose-Hoover thermostat was used. We set six different initial conditions using different random seeds. Although the system reached an equilibrium state at 300 ps, we kept the calculation and obtained three more different equilibrium states at 325, 350, and 400 ps; a total of 24 different equilibrium conditions were prepared. Then, we applied the electric fields of 1.3–1.7 V nm^{-1} to each of the prepared 24 droplets for 30–50 ps, using the microcanonical (NVE) ensemble. We also used shrink-wrapped boundary conditions, where the boundary expands depending on the molecular motions.

The cutoff distance of the LJ potential was conventionally set to be approximately three times the longest distance of σ_{ij}, where the LJ potential is almost zero. On the other hand, the cutoff distance of the Coulomb potential is set to be 100 Å, which is long enough to simulate 4-nm droplets.

Evaluation of ion extraction

In this study, the time step was set to 0.5 fs, and the positions and velocities of each atom were output at every 50 fs to analyze ion extractions. The kinetic energy and the angle of extracted ions were analyzed based on the output images, the position, and the energy of the extracted ions. Here, we assumed that ions were extracted when the ions left the droplet by approximately one or more molecular sizes and when the kinetic energy rose above the equilibrium state. It should be noted that this study focuses only on monomers because more than 90% of extracted ions were monomers. A few percent of dimers and trimers did not break up in a small simulation domain considered. Figure 3 shows the definition of the extracted angle. The extracted angles are defined as the angle between the velocity vector of extracted ions and the direction of the applied electric field, which is in the x-direction. Therefore, the extracted angles are described as

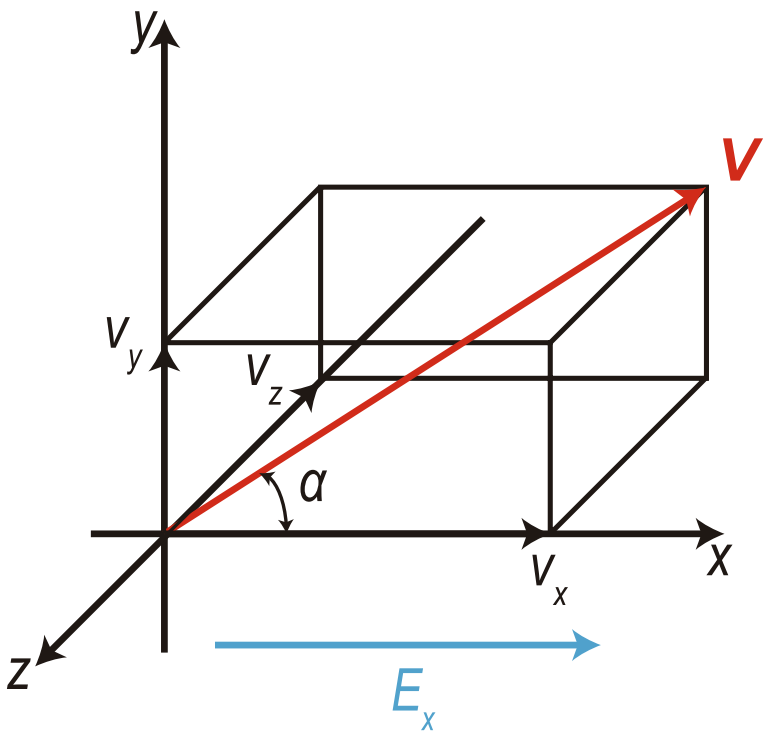

Fig. 3 Definition of the extracted angle *a*

$$\alpha = \cos^{-1}\left(\frac{v_x}{\sqrt{v_x^2 + v_y^2 + v_z^2}}\right). \tag{3}$$

We also employ a solid angle to evaluate ion emission. The solid angle is obtained by assuming that an ionic liquid droplet is a sphere, and the colatitude is defined as the inclination from the line passing through the center of mass and parallel to the x-direction. When only a cation or anion is extracted, the droplet starts to move in the opposite direction. Since the nanodroplet's motion has a non-negligible impact on the following ion emissions, we analyzed ion extraction until the droplet began to move significantly.

Results & discussion

Firstly, we set the cutoff distance of the LJ potential to 12 Å ($>3\sigma_{ij}$) because this is the distance at which the potential is almost zero. Figure 4 shows simulated molecular images of the EMI–BF_4 in an equilibrium state and the state after the electric field has been applied for 15.0 ps after the equilibrium, where the red molecules are cations, and the blue ones are anions. To verify the droplet reached equilibrium, various system properties were investigated. Using the open-source software package TRAVIS [59], the number density profile was calculated for each unique molecule as a function of z distance above and below the x-y plane. As shown in Fig. 5, the observed distribution of cations and anions indicates a well-mixed system and nearly isotropic behavior of molecules within the droplet. Furthermore, the spherical nature of a nanodroplet

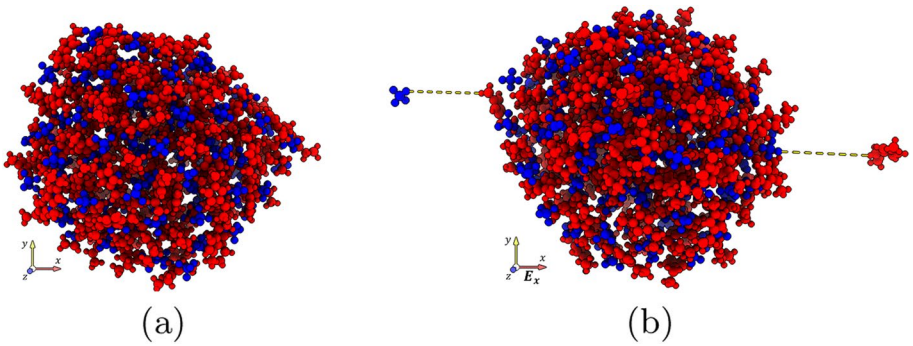

Fig. 4 EMI–BF_4 (**a**) equilibrated droplet and (**b**) a state after electric field has been applied in the positive *x*-direction for ∼15.0 ps. The cations and anions are visualized in red and blue, respectively. Extracted ions are on the order of ∼14 Å

can be assessed based on elements of the moments of inertia tensor [44, 60]. As shown in Fig. 6, after ∼50 ps, the components fluctuate within 5% of an average value and indicate a quasi-spherical state. Lastly, the average radial mass density is shown in Fig. 7 [61]. The interior of the nanodroplet results in bulk-phase densities that are in excellent agreement with the experimental values for EMI–BF_4, 1.28×10^3 kg m^{-3} [62]. The bulk-like behavior drops significantly at the droplet-vacuum interface due to a droplet diameter of ∼4.0 nm. We applied a uniform electric field along the x-direction (the right direction of the image). As shown in Fig. 4, a cation was extracted from the right side of the droplet due to the applied electric field. The distance between the extracted cation and the droplet was approximately 14 Å, which is equal to the molecular size of EMI–BF_4 and EMI–Im.

In the following analysis, only monomers and dimers are considered as extracted ions. The population fraction of species extracted from the droplet for EMI^+-$[EMI–Im]_n$ is shown in Fig. 8 and compared with previous modeling and experimental results. The

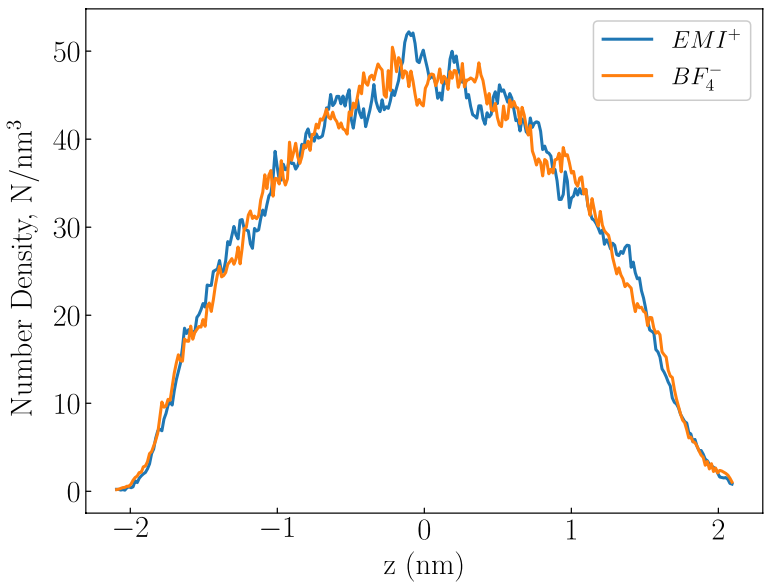

Fig. 5 EMI–BF_4 number density as a function of *z*

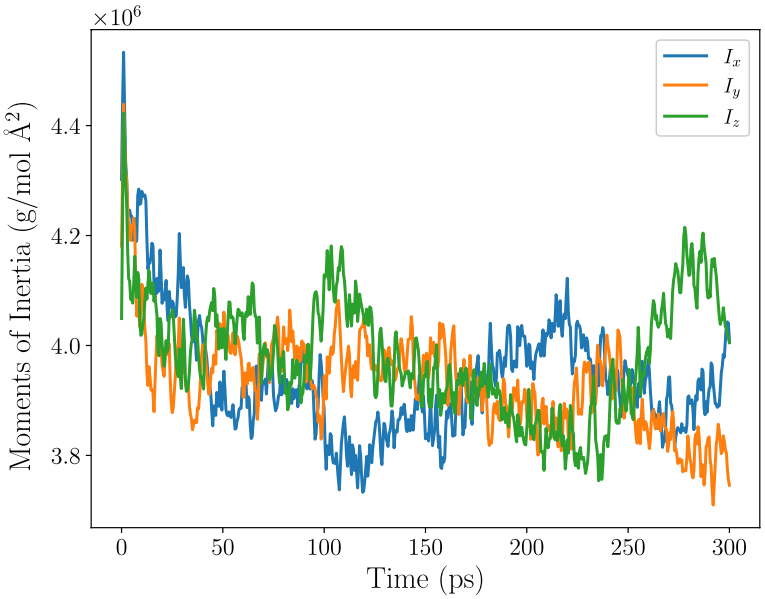

Fig. 6 EMI–BF_4 droplet moments of inertia as a function of time

present study is in excellent agreement with similar MD simulation results provided by Prince et al. [44] and the slight discrepancy can be accounted for by the difference in electric field strength, where the stronger electric field of 1.5 V nm^{-1} results in a greater fraction of n=0 ions, or monomers. Both literature and present modeling results show greater fractions of monomers than the experimental results, which are taken from mass spectrometry and retarding potential analyzer (RPA) measurements from Ticknor et al. [63] and Lozano [64]. The same trend is given in Fig. 9 for EMI^+-[EMI–BF_4] based on experimental results by Natisin et al. [65] and Chen et al. [66].

A few hypotheses arise to explain the increased number of dimer and trimers shown experimentally that are not accounted for in the MD simulations. First, Prince

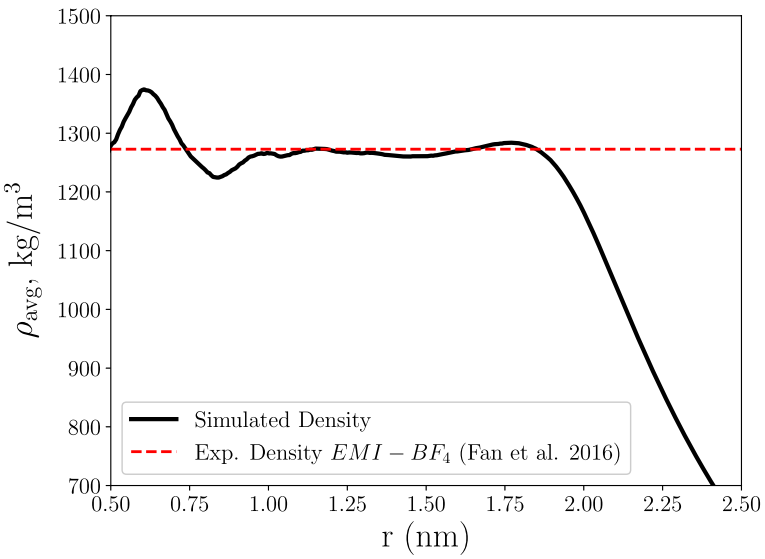

Fig. 7 EMI–BF_4 droplet density as a function of radial distance

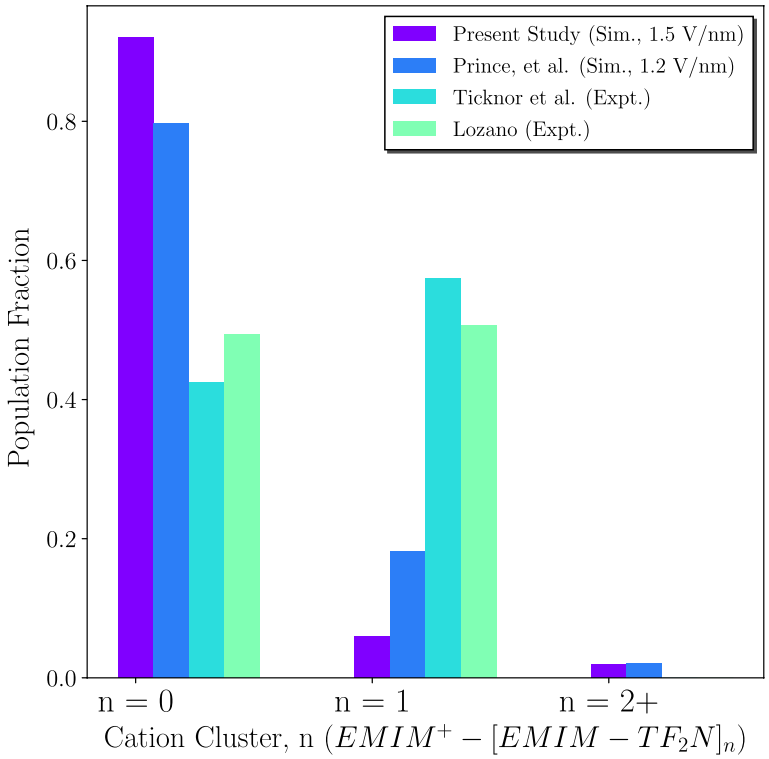

Fig. 8 Emitted species population fraction compared with literature-produced experimental and modeling values for EMI-Im

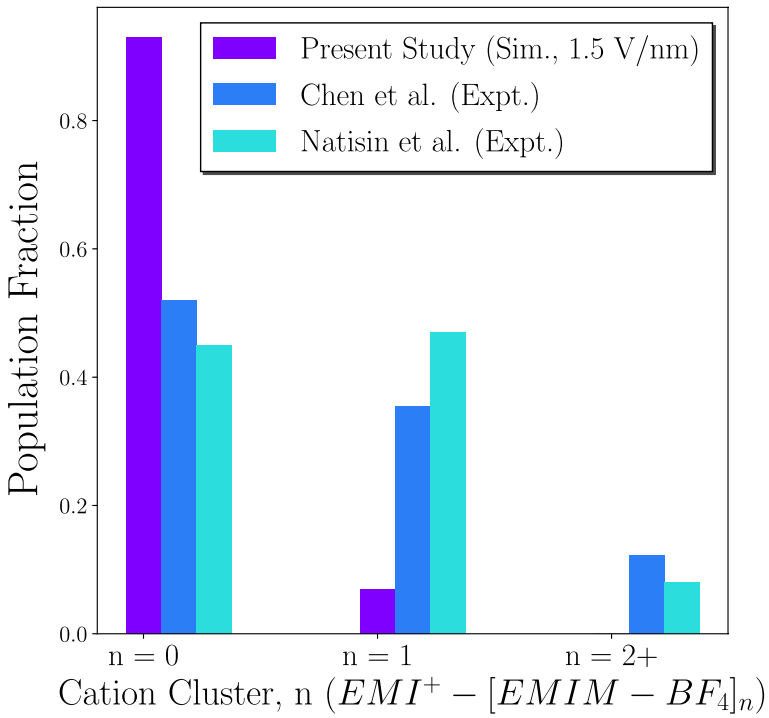

Fig. 9 Emitted species population fraction compared with literature-produced experimental and modeling values for EMI-BF_4

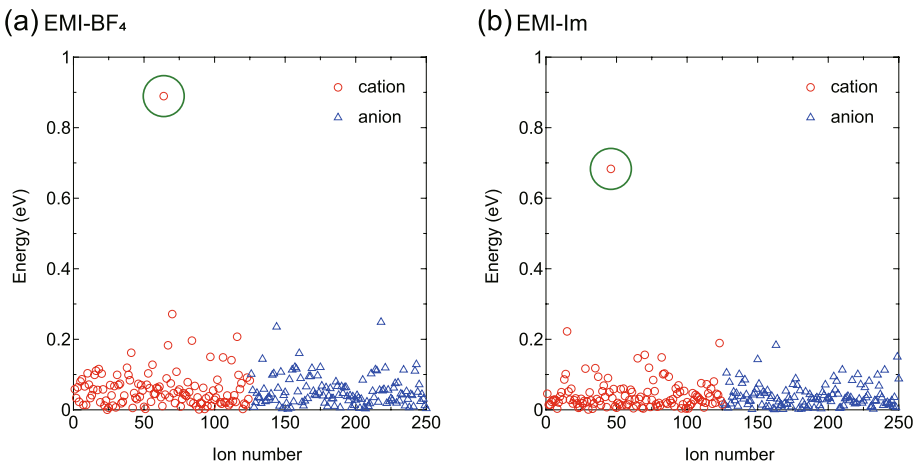

Fig. 10 The energy state of each droplet

et al. note that emission behavior and the angle-resolved species may be especially sensitive to the emitter tip aspect ratio [44]. Moreover, it is noted that both MD simulations from Fig. 8 are using nonpolarizable force fields. In contrast, polarizable simulations capture local electric field effects that may strengthen Coulombic interactions and screen repulsive forces between cation-anion pairs; these effects have shown to be crucial in order to accurately model ionic liquid thermophysical properties [67]. In a comparative study by Yan et al. [68], nonpolarizable simulations of an imadazolium-based ionic liquid over-predicted surface tension by nearly 20 mN m^{-1}. With higher surface tensions, nonpolarizable simulations may artificially suppress the evaporation of large solvated ion clusters and neutrals from the nanodroplet surface. Therefore, it is likely that polarizable simulations may result in higher numbers of dimers and trimers that would compare more favorably with experimental data. Regarding neutral species, while measurements are limited in the literature and are not a part of this effort, future simulations could be used to investigate the reported anomalous mass loss [10] that may hinder electrospray performance.

Figure 10 shows the energy of each ion constituting the droplet of ionic liquid when one of the cations is extracted. The horizontal axis indicates the ion number assigned to each ion in the MD simulation, and the vertical axis indicates the energy of each ion. The red marker within the green circle of Fig. 10 represents the cation extracted and leaving the droplet. Although some cations and anions have energies over 0.2 eV, those ions do not have enough energy to be extracted and remain in the droplet.

Figure 11 shows the time variation of the kinetic energy of the extracted cation of EMI–BF_4 at the electric field of 1.5 V nm^{-1}. Since the kinetic energy continuously changed, we could not determine the kinetic energy threshold when the ion was extracted. In this study, we judged whether the ion was extracted by comparing the output image with the value of the kinetic energy. As mentioned earlier, the ion was assumed to be extracted when the distance between the ion and the droplet was more than one or more molecular sizes. In the present case, the intermolecular distance was approximately 14 Å (Fig. 4), and this value exceeded the cutoff distance of the LJ potential (12 Å), which determined the short-range interaction between molecules.

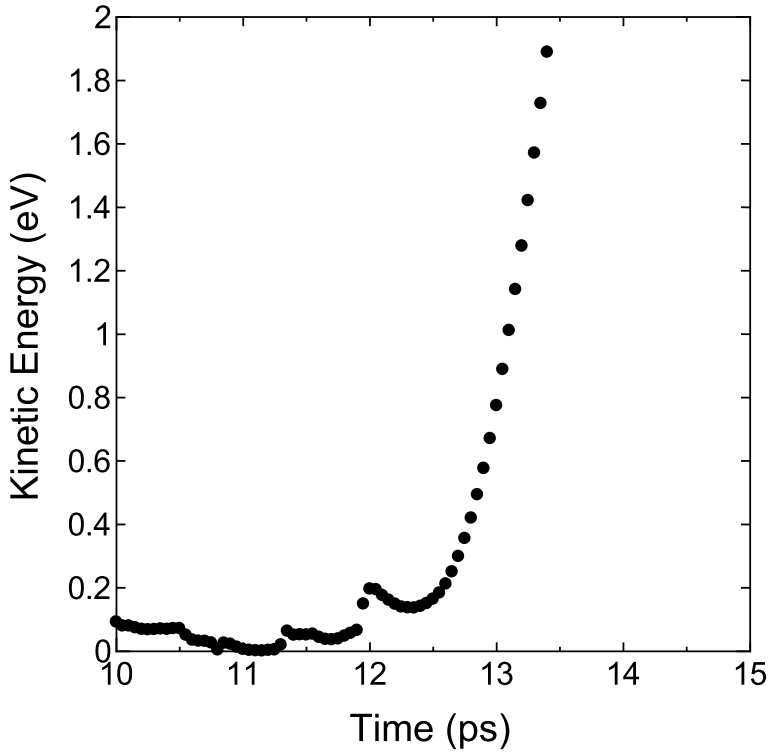

Fig. 11 Time variation of the kinetic energy of an EMI–BF_4 cation at the electric field of 1.5 V nm^{-1}

Beyond the cutoff distance of the LJ potential, only the uniform electric field and the Coulomb potential are applied to ions except for the intramolecular potential, and the uniform electric field of 1.3–1.7 V nm^{-1} is larger than the Coulomb force at 14 Å. Therefore, ions did not return to the droplet when the distance between the extracted ion and the droplet exceeded the cutoff distance of the LJ potential. As mentioned in the "Nanodroplet simulation procedure and equilibration" section, the data was output every 50 fs for the extraction process. Thus, we have uncertainty depending on this time frame. The uncertainty in energy is 0.1–0.2 eV and that in angle is 1°–2°, depending on the output data at 50 fs earlier or later.

The ion kinetic energies are consistent with previously developed theory on ion evaporation and dissociation. Originally postulated by Iribarne and Thomson [69], the evaporative flux of charged particles from a droplet surface is defined by

$$j = \sigma \frac{kT}{h} \exp\left[-\frac{1}{kT}\left(\Delta G_0 - \sqrt{\frac{q^3 E}{4\pi\epsilon_0}}\right)\right], \tag{4}$$

where σ is the surface charge density, k is Boltzmann's constant, T is the system temperature, h is Planck's constant, ΔG_0 is the energy barrier for the particle of charge q to be emitted from the surface, and E is the electric field strength. For common ionic liquids, $\Delta G_0 \sim$ 1–2 eV [70], thus requiring $E \sim$ 1–2 V nm^{-1} for ion emission, as observed in the presented results.

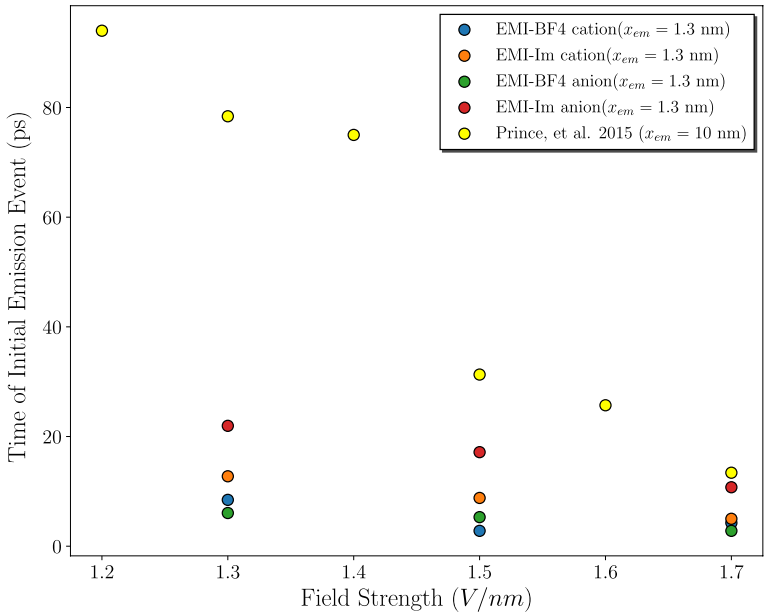

Fig. 12 Comparison of initial emission event as a function of electric field strength

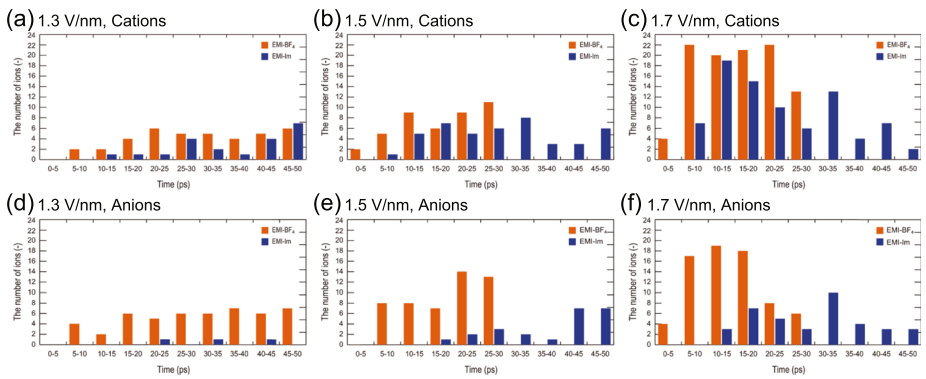

Fig. 13 Number of ions extracted every 5 ps after the electric field is applied

We counted the number of ions extracted every 5 ps after applying the uniform electric field and investigated how easily cations and anions were extracted from EMI–BF_4 and EMI–Im droplets to validate our MD simulations. The time until the first emission event was recorded for each case and compared with results from Prince et al. in Fig. 12. It is noted that the Prince et al. simulations used a detection plane located 10 nm away from the droplet surface, thus accounting for the difference in timescale magnitudes. All simulations show that with increased electric field strength, the time for an emission event to occur decreases monotonically. The comparison between EMI–Im and EMI–BF_4 can be explained by their fundamental difference in electrical conductivity as well as molecular level theory. The EMI–Im anion, often denoted as $[TF_2N]^-$, is a relatively bulky molecule compared to the BF_4^- anion, resulting in EMI–Im cation-anion configurations that experience stronger, longer lasting interactions between the imadazolium-ring hydrogens and the $[TF_2N]^-$ charged atoms [71]. In effect, the EMI–BF_4 molecules

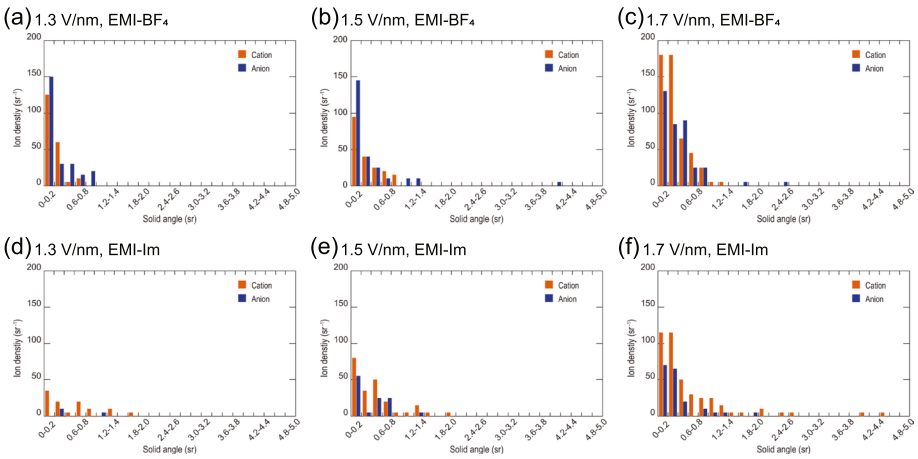

Fig. 14 Number of ions extracted every 0.2 sr

can experience faster rotational and translational motion, especially in response to an external electric field. Figure 12 also shows that these differences between EMI–Im and EMI–BF_4 become less apparent at stronger electric field strengths.

Since the droplet could not keep the shape as time passed after ion extraction, the measurement time was set at up to 50 ps. Figure 13 shows the number of ions extracted for every 5 ps for different applied electric fields of 1.3–1.7 V nm^{-1}. Note that the calculation time was set to 30 ps for EMI–BF_4 at the electric fields of 1.5 and 1.7 V nm^{-1} because the EMI–BF_4 droplet could not keep the shape and was broken up into smaller pieces under the strong electric field after approximately 30 ps. As shown in Fig. 13(a)-(c), the cation of EMI–BF_4 started to be extracted in a few picoseconds after the uniform electric field was applied, while EMI–Im cations tended to be extracted slowly. When the applied electric field increased, the time of the ion extraction decreased for both EMI–BF_4 and EMI–Im. Compared with EMI–Im, a large number of EMI–BF_4 cations were extracted within 30 ps, although the cation of EMI–BF_4 is the same as that of EMI–Im. Regarding the anions (Fig. 13(d)–(f)), EMI–Im anions are much less extracted than EMI–BF_4 anions. Since the electrical conductivity of EMI–BF_4 (1.57 S m^{-1}) is higher than that of EMI–Im (0.91 S m^{-1}), the extracted current of EMI–BF_4 is higher than that of EMI–Im in experiments. The tendency of the MD simulations is in reasonable agreement with the experimental one.

Figure 14 shows the number of ions extracted per steradian as a function of solid angle for both EMI–BF_4 and EMI–Im at the applied electric fields of 1.3, 1.5, and 1.7 V nm^{-1}. As shown in the figure, most ions are extracted around 0 sr, and the solid angle increases when increasing the applied electric field. Compared with EMI–Im cations and anions, more ions are extracted around 0 sr for EMI–BF_4. This tendency is summarized in Table 1. Approximately 60% of both EMI^+ and BF_4^- ions are extracted within 0.2 sr (14.5°) at 1.3 V nm^{-1} for EMI–BF_4, while 92% of EMI^+ ions and 73% of BF_4^- ion are extracted within 0.4 sr (20.6°). The percentage decreases when increasing the applied electric field.

These values for EMI–Im cations and anions tend to be lower than those for EMI–BF_4. Since the number of EMI–Im ions extracted is smaller than that of EMI–BF_4 ions as shown in Fig. 13, the percentage varies more widely for EMI–Im. Nonetheless, the percentage also tends to decrease when increasing the applied electric field, and the values of EMI–Im are lower than those of EMI–BF_4. This tendency is probably because EMI–Im ions take longer to be extracted than EMI–BF_4 as shown in Fig. 13, indicating that the droplet shape tends to be deformed by the applied electric field before ions are extracted.

Furthermore, the extracted angle of EMI–BF_4 tends to increase when increasing the applied electric field, indicating the active motion of ionic liquid droplets. The resultant high-energy ions are produced; then, the off-axis velocity components also increase. However, the extracted angle of EMI–Im tends to decrease when increasing the applied electric field. As shown in Fig. 13, EMI–Im ions take longer to be extracted than EMI–BF_4, and therefore, extracted ions have enough time to face the same direction of the applied electric field before extraction while the ionic liquid droplet has been affected by the electric field. Although most ions are extracted within the solid angle of 0.4 sr (20.6°), such ions can also obtain large extracted angles over 20°, which affects the ion beam trajectory and leads to collisions against the extractor electrode.

The influence of electric field strength on the off-axis velocity component can also be illustrated in the polar plots shown in Fig. 15. For the cation cases in Fig. 15(b)(d), the average angle decreases when the electric field strength increases from 1.3 V nm^{-1} to 1.5 V nm^{-1} and then increases at 1.7 V nm^{-1}. Past the critical electric field strength of 1.5 V nm^{-1}, the nanodroplet begins to fracture and breakup into multiple, satellite droplets, thus creating a subsequent increase in the velocity angle histogram. This phenomenon was also observed by Prince et al. Overall, Fig. 15 indicates that ion extraction dynamics under the explored electric field strengths is more directional than a Lambertian cosine emission (that would peak at 45 degrees).

Figure 16(a)–(c) show the distributions of the extracted angle and the kinetic energy of cations for both EMI–BF_4 and EMI–Im. The average and standard deviation of the kinetic energy are summarized in Table 2. Here, the standard deviation of EMI–Im anion is not shown because only three anions were extracted during the time examined. The averaged kinetic energy of the extracted cation is in the range 0.77–1.20 eV for EMI–BF_4 and 0.67–0.91 eV for EMI–Im, with a slight increase as the electric field increases. Since the surface tension of the EMI–BF_4 and EMI–Im is 50.3 mN m^{-1} and 33.2 mN m^{-1}, respectively, and electrospray phenomena occur when electrostatic pressure is higher than the internal pressure by the surface tension, the difference in kinetic energy is derived from the difference in surface tension. Regarding the anions, EMI–BF_4 indicates a similar tendency compared with its cations, showing a slight increase in kinetic energy when increasing the applied electric field. Because the anions of EMI–Im are hard to extract as shown in Fig. 13(d)–(f), they need much more time for the extraction after the electric field is applied. This long-time electric field application causes an increase in the internal energy of EMI–Im droplet and the resultant high kinetic energy of extracted anions of EMI–Im, which is comparable to that of EMI–BF_4 anions. It should be noted again that the droplet was charged due to ion extraction, and then

Table 1 The ratio of ions extracted within a solid angle

		1.3 V/nm		1.5 V/nm		1.7 V/nm	
		0.2 sr	0.4 sr	0.2 sr	0.4 sr	0.2 sr	0.4 sr
EMI-BF_4	EMI^+	62%	92%	49%	69%	36%	71%
	BF_4^-	61%	73%	59%	75%	36%	59%
EMI-Im	EMI^+	33%	52%	36%	52%	27%	55%
	Im^-	0%	67%	48%	52%	39%	75%

it started to move in the opposite direction of the electric field. It is desirable to fix the droplet or set the wall and prevent the droplet from moving; this work will be performed in the future.

Conclusion

We have conducted molecular dynamics simulations of the ionic liquid electrospray thruster and investigated extracted energies and angles from an approximately 4–5 nm droplet under the uniform electric field condition of 1.3–1.7 V nm^{-1}. In this study, we employed EMI–BF_4 and EMI–Im as the propellant. When we counted the number of ions extracted every 5 ps, we found that EMI–BF_4 was easier to extract than EMI–Im for both anions and cations. This tendency is in reasonable agreement with experimental results, where EMI–BF_4 has a higher electrical conductivity, leading to a higher current than EMI–Im. The kinetic energy at ion extraction seems to increase slightly with the applied electric field, and EMI–Im with lower surface tension leads to lower initial kinetic energy at the onset of cation extraction than EMI–BF_4. Although most ions were extracted at a small solid angle with respect to the x-direction, which is the same direction of the applied electric field, such ions could also have a relatively large extracted angle because of the active motion in the droplet imparted by the electric field, which probably results in collisions against the extractor electrode.

The primary conclusions can be further summarized as follows:

1. The primary species emitted from the nanodroplet surface are monomers. While this result is in agreement with atomistic simulations that use a similar force field [44], the reason for discrepancy between mass spectrometry and RPA measurements requires further investigation.
2. Energies of extracted ions were on the order of 1–2 eV and matched theoretical expectations.
3. At lower electric field strengths, the differences in EMI–Im and EMI–BF_4 emission behavior can be attributed to the attractive forces between the cation-anion pairs. Namely, EMI–Im exhibited slower initial emission, likely due to the greater hydrogen bond strength between its cations and anions. Moreover, the present study showed higher extracted current profiles for EMI–BF_4 than EMI–Im.
4. Electric field strengths past the critical value of 1.5 V nm^{-1} resulted in an increase in the overall angular velocity distribution of cations for both EMI–Im and EMI–BF_4, indicative of nanodroplet fracturing and breakup.

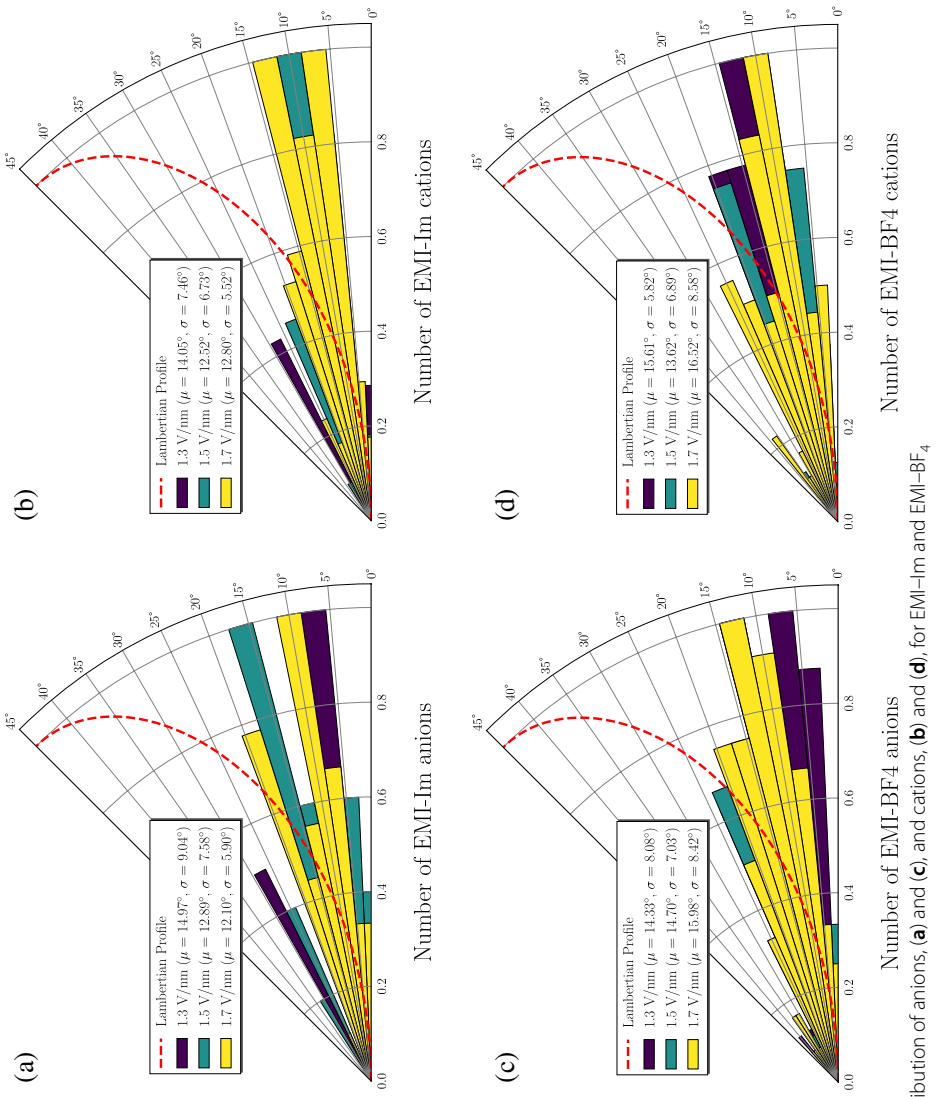

Fig. 15 Normalized angular distribution of anions, (**a**) and (**c**), and cations, (**b**) and (**d**), for EMI–Im and EMI–BF_4

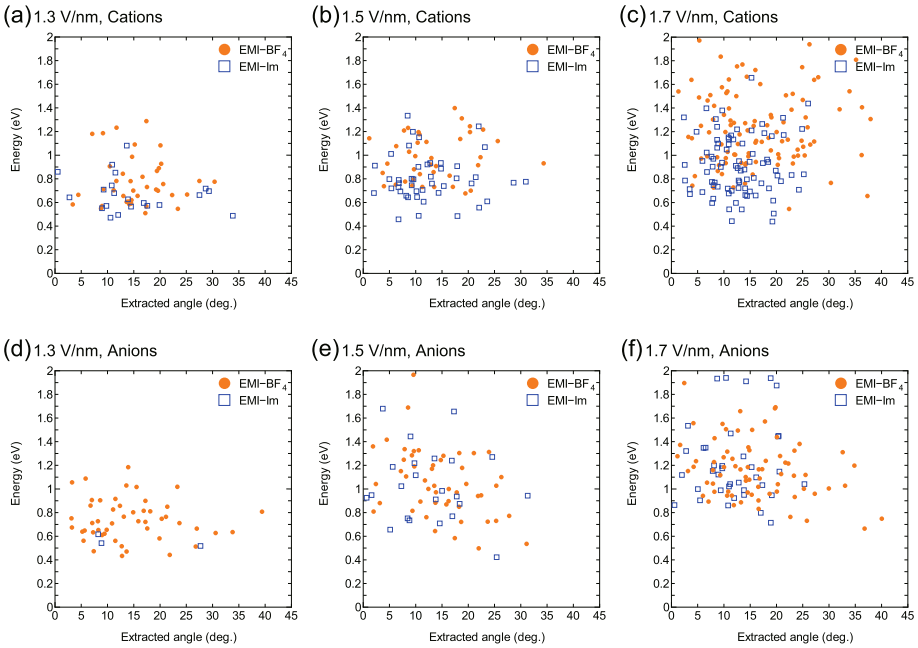

Fig. 16 Distributions of the kinetic energy versus extracted angle

Table 2 Average and standard deviation of kinetic energy for extracted ions

		1.3 V/nm		1.5 V/nm		1.7 V/nm	
		K_{av} (eV)	K_{sd} (eV)	K_{av} (eV)	K_{sd} (eV)	K_{av} (eV)	K_{sd} (eV)
EMI-BF_4	EMI^+	0.77	0.20	0.97	0.19	1.20	0.30
	BF_4^-	0.74	0.17	1.05	0.28	1.16	0.25
EMI-Im	EMI^+	0.67	0.15	0.80	0.19	0.91	0.25
	Im^-	0.56	-	1.05	0.32	1.23	0.34

Acknowledgments
The part of the computer simulations was performed on the A-KDK computer system at the Research Institute for Sustainable Humanosphere, Kyoto University. The authors thank Dr. Anirudh Thuppul, Dr. Peter Wright, and Dr. Adam Collins from UCLA, and Dr. John Ziemer from NASA JPL for their insightful discussions.

Authors' contributions
Conceptualization: Yoshinori Takao; Methodology: Ryohei Yamada and Takaaki Enomoto; Formal analysis: Takaaki Enomoto and Shehan Parmar; Investigation and visualization: Takaaki Enomoto; Supervision and project administration: Richard E. Wirz and Yoshinori Takao; Funding acquisition: Yoshinori Takao and Richard E. Wirz; Writing - original draft preparation, Takaaki Enomoto; Writing - review and editing; Shehan Parmar, Richard E. Wirz, and Yoshinori Takao. All authors read and approved the final manuscript.

Funding
This work was supported in part by JSPS (Japan Society for the Promosion of Science) KAKENHI (Grants-in-Aid for Scientific Research), Grant Numbers JP18H01623 and JP 21H01530, the Canon Foundation, the Asahi Glass Foundation, SEI Group CSR Foundation, Yokohamakogyokai Research Aid Foundation, JAXA/RDD (Japan Aerospace Exploration Agency/Research and Development Directorate), and JST FOREST Program Grant Number JPMJFR2129. This material is based upon work supported by the U.S. Department of Energy, Office of Science, Office of Advanced Scientific Computing Research, Department of Energy Computational Science Graduate Fellowship under Award Number DE-SC0022158. Funding was also provided by NASA's Jet Propulsion Laboratory, California Institute of Technology to support the LISA CMNT development plan (NASA/JPL Award No. 1580267) and the Air Force Office of Scientific Research (AFOSR Award No. FA9550-21-1-0067).

Availability of data and materials

The LAMMPS input scripts and datasets generated during and/or analysed during the current study are available from the corresponding author on reasonable request.

Code availability All the simulations are conducted using the Large-scale Atomic/Molecular Massively Parallel Simulator (LAMMPS) package, which is available from the following URL: https://www.lammps.org/.

Declarations

Competing interests
The authors declare that they have no competing interests.

Received: 21 February 2022 Accepted: 22 July 2022
Published online: 26 September 2022

References

1 SpaceWorks Enterprises, Inc. (2020) Nano/Microsatellite Market Forecast, 10th Edition. https://www.spaceworks.aero/wp-content/uploads/Nano-Microsatellite-Market-Forecast-10th-Edition-2020.pdf. Accessed 24 Aug 2022
2 Poghosyan A, Golkar A (2017) CubeSat evolution: Analyzing CubeSat capabilities for conducting science missions. Prog Aerosp Sci 88:59–83. https://doi.org/10.1016/j.paerosci.2016.11.002.
3 Levchenko I, Bazaka K, Ding Y, Raitses Y, Mazouffre S, Henning T, Klar PJ, Shinohara S, Schein J, Garrigues L, Kim M, Lev D, Taccogna F, Boswell RW, Charles C, Koizumi H, Shen Y, Scharlemann C, Keidar M, Xu S (2018) Space micropropulsion systems for Cubesats and small satellites: From proximate targets to furthermost frontiers. Appl Phys Rev 5(1):11104. https://doi.org/10.1063/1.5007734.
4 Mueller HRZJJ (2010) Survey of Propulsion Technologies Applicable to Cubesats. Technical report. NASA Jet Propulsion Lab, Pasadena.
5 Krejci D, Lozano P (2018) Space Propulsion Technology for Small Spacecraft. Proc IEEE 106(3):362–378. https://doi.org/10.1109/JPROC.2017.2778747.
6 O'Reilly D, Herdrich G, Kavanagh DF (2021) Electric Propulsion Methods for Small Satellites: A Review. https://doi.org/10.3390/aerospace8010022.
7 Taylor GI (1964) Disintegration of water drops in an electric field. Proc R Soc Lond A Math Phys Sci 280(1382):383–397. https://doi.org/10.1098/rspa.1964.0151.
8 Krejci D, Mier-Hicks F, Thomas R, Haag T, Lozano P (2017) Emission Characteristics of Passively Fed Electrospray Microthrusters with Propellant Reservoirs. J Spacecr Rocket 54(2):447–458. https://doi.org/10.2514/1.A33531.
9 Lozano P, Martínez-Sánchez M (2005) Ionic liquid ion sources: characterization of externally wetted emitters. J Colloid Interface Sci 282(2):415–421. https://doi.org/10.1016/j.jcis.2004.08.132.
10 Natisin MR, Zamora HL, Holley ZA, Ivan Arnold N, McGehee WA, Holmes MR, Eckhardt D (2021) Efficiency Mechanisms in Porous-Media Electrospray Thrusters. J Propuls Power 37(5):650–659. https://doi.org/10.2514/1.B38160.
11 Courtney DG (2011) Ionic Liquid Ion Source Emitter Arrays Fabricated on Bulk Porous Substrates for Spacecraft Propulsion. PhD thesis. Massachusetts Institute of Technology.
12 Ziemer J, Gamero-Castaño M, Hruby V, Spence D, Demmons N, McCormick R, Roy T, Gasdaska C, Young J, Connolly B (2005) Colloid Micro-Newton Thruster Development for the ST7-DRS and LISA Missions In: 41st AIAA/ASME/SAE/ASEE Joint Propulsion Conference & Exhibit. Joint Propulsion Conferences.. American Institute of Aeronautics and Astronautics, Tucson. https://doi.org/10.2514/6.2005-4265.
13 Dupont J, de Souza RF, Suarez PAZ (2002) Ionic Liquid (Molten Salt) Phase Organometallic Catalysis. Chem Rev 102(10):3667–3692. https://doi.org/10.1021/cr010338r.
14 Kitazawa Y, Ueno K, Watanabe M (2018) Advanced Materials Based on Polymers and Ionic Liquids. Chem Rec 18(4):391–409. https://doi.org/10.1002/tcr.201700041.
15 Courtney DG, Shea H, Dannenmayer K, Bulit A (2017) Charge Neutralization and Direct Thrust Measurements from Bipolar Pairs of Ionic Electrospray Thrusters. J Spacecr Rocket 55(1):54–65. https://doi.org/10.2514/1.A33863.
16 Krejci D, Jenkins MG, Lozano P (2019) Staging of electric propulsion systems: Enabling an interplanetary Cubesat. Acta Astronaut 160:175–182. https://doi.org/10.1016/j.actaastro.2019.04.031.
17 Ziemer JK, Marrese-Reading C, Arestie SM, Conroy DG, Leifer SD, Lopez Ortega A, Demmons NR, Wirz RE, Gamero MIncorporating Lessons Learned into LISA Colloid Microthruster Technology Development In: AIAA Propulsion and Energy 2019 Forum. AIAA Propulsion and Energy Forum.. American Institute of Aeronautics and Astronautics. https://doi.org/10.2514/6.2019-3814.
18 Wirz RE (2019) Electrospray Thruster Performance and Lifetime Investigation for the LISA Mission In: AIAA Propulsion and Energy 2019 Forum.. American Institute of Aeronautics and Astronautics, Indianapolis. https://doi.org/10.2514/6.2019-3816.

19 Nakagawa K, Tsuchiya T, Takao Y (2017) Microfabricated emitter array for an ionic liquid electrospray thruster. Jpn J Appl Phys 56(6S1):06–18. https://doi.org/10.7567/jjap.56.06gn18.
20 Courtney DG, Li HQ, Lozano P (2012) Emission measurements from planar arrays of porous ionic liquid ion sources. J Phys D Appl Phys 45(48):485203. https://doi.org/10.1088/0022-3727/45/48/485203.
21 Thuppul A, Wright PL, Collins AL, Ziemer JK, Wirz RE (2020) Lifetime Considerations for Electrospray Thrusters. Aerospace 7(8). https://doi.org/10.3390/aerospace7080108.
22 Emoto K, Tsuchiya T, Takao Y (2018) Numerical Investigation of Steady and Transient Ion Beam Extraction Mechanisms for Electrospray Thrusters. Trans Jpn Soc Aeronaut Space Sci Aerosp Technol Jpn 16(2):110–115. https://doi.org/10.2322/tastj.16.110.
23 Nuwal N, Azevedo VA, Klosterman MR, Budaraju S, Levin DA, Rovey JL (2021) Multiscale modeling of fragmentation in an electrospray plume. J Appl Phys 130(18):184903. https://doi.org/10.1063/5.0064711.
24 Ma C, Ryan C (2021) Plume particle energy analysis of an ionic liquid electrospray ion source with high emission density. J Appl Phys 129(8):83302. https://doi.org/10.1063/5.0035889.
25 Liu X, Kang X, Deng H, Sun Y (2021) Energy properties and spatial plume profile of ionic liquid ion sources based on an array of porous metal strips. Plasma Sci Technol 23(12):125502. https://doi.org/10.1088/2058-6272/ac23bd.
26 Gamero-Castaño M (2008) The structure of electrospray beams in vacuum. J Fluid Mech 604:339–368. https://doi.org/10.1017/S0022112008001316.
27 Parmar SM, Collins AL, Wirz RE (2021) Electrospray Plume Modeling for Rapid Life and Performance Analysis In: AIAA SciTech Forum.. American Institute of Aeronautics and Astronautics, San Diego. https://doi.org/10.2514/6.2022-1357.
28 Zhao Y, Zhao J-S, Zhao F-Q, Xu S-Y, Ju X-H (2020) Revealing the decomposition behavior of hexanitrostilbene and aluminum nanoparticles composites: A reactive molecular dynamics simulation. Acta Astronaut 177:320–331. https://doi.org/10.1016/j.actaastro.2020.07.042.
29 Ray P, Balducci A, Kirchner B (2018) Molecular Dynamics Simulations of Lithium-Doped Ionic-Liquid Electrolytes. J Phys Chem B 122(46):10535–10547. https://doi.org/10.1021/acs.jpcb.8b06022.
30 Malali S, Foroutan M (2017) Study of Wetting Behavior of BMIM+/PF6– Ionic Liquid on TiO2 (110) Surface by Molecular Dynamics Simulation. J Phys Chem C 121(21):11226–11233. https://doi.org/10.1021/acs.jpcc.6b12065.
31 Torfason K, Valfells A, Manolescu A (2016) Molecular dynamics simulations of field emission from a prolate spheroidal tip. Phys Plasmas 23(12):123119. https://doi.org/10.1063/1.4972821.
32 Saiz F, Gamero-Castaño M (2016) Molecular dynamics of nanodroplet impact: The effect of the projectile's molecular mass on sputtering. AIP Adv 6(6):65319. https://doi.org/10.1063/1.4954740.
33 Nakazaki N, Takao Y, Eriguchi K, Ono K (2015) Molecular dynamics simulations of Si etching in Cl- and Br-based plasmas: Cl+ and Br+ ion incidence in the presence of Cl and Br neutrals. J Appl Phys 118(23):233304. https://doi.org/10.1063/1.4937449.
34 Daily JW, Micci MM (2009) Ionic velocities in an ionic liquid under high electric fields using all-atom and coarse-grained force field molecular dynamics. J Chem Phys 131(9):94501. https://doi.org/10.1063/1.3197850.
35 Daily JW (2008) Molecular Dynamics Simulation of Ion Emission from Nanodroplets of Ionic Liquids. J Propuls Power 24(5):981–986. https://doi.org/10.2514/1.28762.
36 Bobrov AA, Bronin SY, Klyarfeld AB, Zelener BB, Zelener BV (2020) Molecular dynamics calculation of thermal conductivity and shear viscosity in two-component fully ionized strongly coupled plasma. Phys Plasmas 27(1):10701. https://doi.org/10.1063/1.5128446.
37 Borner A, Li Z, Levin DA (2012) Modeling of an ionic liquid electrospray using molecular dynamics with constraints. J Chem Phys 136(12):124507. https://doi.org/10.1063/1.3696006.
38 Ghalami F, Sedghamiz T, Sedghamiz E, Khashei F, Zahedi E (2019) Molecular Dynamics Simulation of Wetting and Interfacial Properties of Multicationic Ionic Liquid Nanodroplets on Boron Nitride Monolayers: A Comparative Approach. J Phys Chem C 123(22):13551–13560. https://doi.org/10.1021/acs.jpcc.8b11987.
39 Zhang J, Cai G, Liu X, He B, Wang W (2021) Molecular dynamics simulation of ionic liquid electrospray: Revealing the effects of interaction potential models. Acta Astronaut 179:581–593. https://doi.org/10.1016/j.actaastro.2020.11.018.
40 Zheng F, Zhang S, Mo J, Yi H, Zhang S, Yu H, Lin K, Sha J, Chen Y (2020) Ion Concentration Effect on Nanoscale Electrospray Modes. Small 16(24):2000397. https://doi.org/10.1002/smll.202000397.
41 Borner A, Levin DA (2015) Coupled Molecular Dynamics—3-D Poisson Simulations of Ionic Liquid Electrospray Thrusters. IEEE Trans Plasma Sci 43(1):295–304. https://doi.org/10.1109/TPS.2014.2327913.
42 Borner A, Wang P, Levin DA (2014) Influence of electrical boundary conditions on molecular dynamics simulations of ionic liquid electrosprays. Phys Rev E 90(6):63303. https://doi.org/10.1103/PhysRevE.90.063303.
43 Kim DY, Micci MM (2013) Molecular Dynamics Simulations of a Liquid Gallium Electrospray Thruster. J Propuls Power 29(4):899–905. https://doi.org/10.2514/1.B34501.
44 Prince BD, Tiruppathi P, Bemish RJ, Chiu Y-H, Maginn EJ (2015) Molecular Dynamics Simulations of 1-Ethyl-3-methylimidazolium Bis[(trifluoromethyl)sulfonyl]imide Clusters and Nanodrops. J Phys Chem A 119(2):352–368. https://doi.org/10.1021/jp507073e.
45 Plimpton S (1995) Fast Parallel Algorithms for Short-Range Molecular Dynamics. J Comput Phys 117(1):1–19. https://doi.org/10.1006/jcph.1995.1039.
46 Martínez L, Andrade R, Birgin EG, Martínez JM (2009) PACKMOL: A package for building initial configurations for molecular dynamics simulations. J Comput Chem 30(13):2157–2164. https://doi.org/10.1002/jcc.21224.
47 Martínez JM, Martínez L (2003) Packing optimization for automated generation of complex system's initial configurations for molecular dynamics and docking. J Comput Chem 24(7):819–825. https://doi.org/10.1002/jcc.10216.
48 Allen MP, Tildesley DJ (2017) Computer Simulation of Liquids. 2nd edn.. Oxford University Press, New York.
49 Wang Y, Noid WG, Liu P, Voth GA (2009) Effective force coarse-graining. Phys Chem Chem Phys 11(12):2002–2015. https://doi.org/10.1039/B819182D.
50 Takahashi N (2010) Molecular dynamics modeling of ionic liquids in electrospray propulsion. Master thesis. https://dspace.mit.edu/handle/1721.1/59700. Accessed 24 Aug 2022

51 Coles T, Fedkiw T, Lozano P (2012) Investigating Ion Fragmentation in Electrospray Thruster Beams In: 48th AIAA/ASME/SAE/ASEE Joint Propulsion Conference & Exhibit.. American Institute of Aeronautics and Astronautics, Atlanta. https://doi.org/10.2514/6.2012-3793.
52 Villanueva-Bonay E, Gamero-Castaño M (2019) Molecular dynamics of nanodroplet impact: The effect of particle resolution in the projectile model. AIP Advances 9(8):85204. https://doi.org/10.1063/1.5100964.
53 Hunt PA (2006) The simulation of imidazolium-based ionic liquids. Mol Simul 32(1):1–10. https://doi.org/10.1080/08927020500486627.
54 Bedrov D, Piquemal JP, Borodin O, MacKerell AD, Roux B, Schröder C (2019) Molecular Dynamics Simulations of Ionic Liquids and Electrolytes Using Polarizable Force Fields. Am Chem Soc. https://doi.org/10.1021/acs.chemrev.8b00763. https://pubs.acs.org/sharingguidelines.
55 Islam MM, Kolesov G, Verstraelen T, Kaxiras E, van Duin ACT (2016) eReaxFF: A Pseudoclassical Treatment of Explicit Electrons within Reactive Force Field Simulations. J Chem Theory Comput 12(8):3463–3472. https://doi.org/10.1021/acs.jctc.6b00432.
56 Jorgensen WL, Maxwell DS, Tirado-Rives J (1996) Development and Testing of the OPLS All-Atom Force Field on Conformational Energetics and Properties of Organic Liquids. J Am Chem Soc 118(45):11225–11236. https://doi.org/10.1021/ja9621760.
57 Canongia Lopes JN, Pádua AAH, Shimizu K (2008) Molecular Force Field for Ionic Liquids IV: Trialkylimidazolium and Alkoxycarbonyl-Imidazolium Cations; Alkylsulfonate and Alkylsulfate Anions. J Phys Chem B 112(16):5039–5046. https://doi.org/10.1021/jp800281e.
58 Chiu Y-H, Gaeta G, Levandier DJ, Dressler RA, Boatz JA (2007) Vacuum electrospray ionization study of the ionic liquid, [Emim][Im]. Int J Mass Spectrom 265(2):146–158. https://doi.org/10.1016/j.ijms.2007.02.010.
59 Brehm M, Thomas M, Gehrke S, Kirchner B (2020) TRAVIS—A free analyzer for trajectories from molecular simulation. J Chem Phys 152(16):164105. https://doi.org/10.1063/5.0005078.
60 Malek SMA, Poole PH, Saika-Voivod I (2018) Thermodynamic and structural anomalies of water nanodroplets. Nat Commun 9(1):2402. https://doi.org/10.1038/s41467-018-04816-2.
61 Leong K-Y, Wang F (2018) A molecular dynamics investigation of the surface tension of water nanodroplets and a new technique for local pressure determination through density correlation. J Chem Phys 148(14):144503. https://doi.org/10.1063/1.5004985.
62 Fan X-H, Chen Y-P, Su C-S (2016) Density and Viscosity Measurements for Binary Mixtures of 1-Ethyl-3-methylimidazolium Tetrafluoroborate ([Emim][BF4]) with Dimethylacetamide, Dimethylformamide, and Dimethyl Sulfoxide. J Chem Eng Data 61(2):920–927. https://doi.org/10.1021/acs.jced.5b00753.
63 Ticknor B, Anderson J, Fritz B, Chiu Y-H (2010) Effect of Aspect Ratio on the Wettability and Electrospray Properties of Porous Tungsten Emitters with the Ionic Liquid [Emim][Im] In: 46th AIAA/ASME/SAE/ASEE Joint Propulsion Conference & Exhibit.. American Institute of Aeronautics and Astronautics, Nashville. https://doi.org/10.2514/6.2010-6618.
64 Lozano PC (2005) Energy properties of an EMI-Im ionic liquid ion source. J Phys D Appl Phys 39(1):126–134. https://doi.org/10.1088/0022-3727/39/1/020.
65 Natisin MR, Zamora HL, McGehee WA, Arnold NI, Holley ZA, Holmes MR, Eckhardt D (2020) Fabrication and characterization of a fully conventionally machined, high-performance porous-media electrospray thruster. J Micromech Microeng 30(11):115021. https://doi.org/10.1088/1361-6439/abb8c3.
66 Chen C, Chen M, Zhou H (2020) Characterization of an ionic liquid electrospray thruster with a porous ceramic emitter. Plasma Sci Technol 22(9):94009. https://doi.org/10.1088/2058-6272/ab9528.
67 Bedrov D, Piquemal J-P, Borodin O, MacKerell AD, Roux B, Schröder C (2019) Molecular Dynamics Simulations of Ionic Liquids and Electrolytes Using Polarizable Force Fields. Chem Rev 119(13):7940–7995. https://doi.org/10.1021/acs.chemrev.8b00763.
68 Yan T, Li S, Jiang W, Gao X, Xiang B, Voth GA (2006) Structure of the LiquidVacuum Interface of Room-Temperature Ionic Liquids: A Molecular Dynamics Study. J Phys Chem B 110(4):1800–1806. https://doi.org/10.1021/jp055890p.
69 Iribarne JV, Thomson BA (1976) On the evaporation of small ions from charged droplets. J Chem Phys 64(6):2287–2294. https://doi.org/10.1063/1.432536.
70 Gamero-Castaño M, Fernández de la Mora J (2000) Direct measurement of ion evaporation kinetics from electrified liquid surfaces. J Chem Phys 113(2):815–832. https://doi.org/10.1063/1.481857.
71 Qiao B, Krekeler C, Berger R, Delle Site L, Holm C (2008) Effect of Anions on Static Orientational Correlations, Hydrogen Bonds, and Dynamics in Ionic Liquids: A Simulational Study. J Phys Chem B 112(6):1743–1751. https://doi.org/10.1021/jp0759067.

Publisher's Note